IOP Conference Series:
Earth and
Environmental Science

PURPOSE-LED PUBLISHING™

PAPER • **OPEN ACCESS**

Numerical prediction of the fluid damping of a standing disc with a variable axial distance from a rigid wall

To cite this article: K Khalfaoui *et al* 2024 *IOP Conf. Ser.: Earth Environ. Sci.* **1411** 012041

View the article online for updates and enhancements.

You may also like

- A novel energy harvesting device for self-monitoring wireless sensor node in fluid dampers
Si Qi Wang, Miao Yu, Jie Fu et al.
- Numerical and experimental study of a novel GER fluid damper based on helical duct flow
Jinglei Zhao, Xijun Cao, Yan Jing et al.
- Design, testing and modelling of a tuneable GER fluid damper under shear mode
Yi Sun, Yining Huang, Min Wang et al.



This content was downloaded from IP address 79.155.11.128 on 09/04/2025 at 09:35

IOP Conf. Series: Earth and Environmental Science **1411** (2024) 012041 doi:10.1088/1755-1315/1411/1/012041

Numerical prediction of the fluid damping of a standing disc with a variable axial distance from a rigid wall

K Khalfaoui[1,3], G Moraga[2], J Bareis[1], M Zorn[1], A Presas[2] and S Riedelbauch[1]

[1] Institute of Fluid Mechanics and Hydraulic Machinery (IHS), University of Stuttgart, Pfaffenwaldring 10, 70569 Stuttgart, Germany
[2] Centre for Industrial Diagnostics and Fluid Dynamics (CDIF) – Universitat Poltècnica de Catalunya, Av. Diagonal, 647 08028 Barcelona, Spain

[3] Corresponding author, email adress: karim.khalfaoui@ihs.uni-stuttgart.de

Abstract. Near-resonant flow-induced vibrations are a significant cause of fatigue damage in hydraulic impellers. The amplitude of these vibrations is limited mainly by the fluid damping, making its quantification paramount for the safety of hydraulic turbines. To study the fluid damping for low-specific-speed radial impellers, a submerged disc in still water with a variable vertical distance from a rigid wall is investigated. This setup serves as an abstraction of the axial gap between impeller hub and head cover, and of the modal behavior of impellers for the case of diametrical nodal lines. The fluid damping is computed numerically for the 3-nodal-diameters mode using the imposed modal motion approach for various axial gap sizes and vibration amplitudes. The results are contrasted with the experimental damping measured with the same setup. First, a simulation configuration that accurately replicates the experimentally measured damping in value and tendency is presented. The factors that would normally impede a valid numerical prediction are exposed and solutions are suggested. Second, the valid simulation results are thoroughly studied, and the flow field is visualized to gain insight into the physical mechanisms that cause the fluid mass and damping. As a result, the interaction between fluid and structure in this system is understood.

1. Introduction

The higher penetration of the energy mix by wind and solar powerplants has been posing higher flexibility requirements on hydropower plants, leading to an increase in off-design operation and more frequent start-stop sequences. This change in the operation routines leads to an increase of mechanical loads that cause fatigue damage [1]. Low-load conditions are associated with increased dynamic stresses, sometimes as a result of near-resonant vibration [2]. Therefore, it is indispensable to accurately predict the structural vibrations for a reliable fatigue life assessment and a safe operation of hydraulic turbines.

The vibration behavior of hydraulic turbines is heavily influenced by the surrounding fluid. The interaction between the vibrating structure and the surrounding fluid induces a fluid reaction force on the structure. This force is caused by the perturbation induced by the vibrating structure itself. Applying linear dynamics theory and a set of simplifications, the latter force can be modelled by an added mass effect, an added damping effect and an added stiffness effect on a modal basis. That is, the fluid force is perceived as a change of the mass, damping and stiffness of the structure. This yields a surrogate modal oscillator of which the equation of motion can be written in the form of equations (1,2):

Content from this work may be used under the terms of the Creative Commons Attribution 4.0 licence. Any further distribution of this work must maintain attribution to the author(s) and the title of the work, journal citation and DOI.
Published under licence by IOP Publishing Ltd

$$\left(m_k + m_{k,Fluid}\right)\ddot{\eta}_k + \left(c_k + c_{k,Fluid}\right)\dot{\eta}_k + \left(k_k + k_{k,Fluid}\right)\eta_k = \underline{\varphi_k}^T \underline{f_{1,Fluid}} \quad (1)$$

$$\underline{\varphi_k}^T \underline{f_{2,Fluid}} = -m_{k,Fluid}\ddot{\eta}_k - c_{k,Fluid}\dot{\eta}_k - k_{k,Fluid}\eta_k \quad (2)$$

Here, m_k, $m_{k,Fluid}$, c_k, $c_{k,Fluid}$, k_k, $k_{k,Fluid}$, η_k, $\underline{\varphi_k}$, overdot (⃜), and $\underline{f_{1,Fluid}}$ denote respectively the structural modal mass, the fluid modal mass, the structural modal damping, the fluid modal damping, the structural modal stiffness, the fluid modal stiffness, the modal coordinate, the mode shape vector of a spatially discrete structure, temporal derivation, and the fluid excitation force (rooted purely in the flow behavior). The fluid modal quantities described in equation (1) are commonly designated as added mass, added damping, and added stiffness. Equation (2) describes the vibration-induced fluid force $\underline{f_{2,Fluid}}$, which combines the fluid added quantities. The expression is already inserted into equation (1).

Near-resonant vibration amplitudes are limited by the damping which comes primarily from the fluid in hydraulic turbines. Therefore, the prediction of fluid-added damping is of particular importance [3,4]. Multiple works addressed the fluid-added damping in blade channels of hydraulic impellers by studying systems ranging from hydrofoils to entire Francis turbines [5–12]. However, the impact of the impeller side chambers, that is the gap between head cover and impeller hub, and the gap between shroud and cone, has only gotten little attention.

Low-specific-speed radial impellers resemble in their shape discs and thus exhibit disc-like mode shapes characterized by diametrical vibration nodes (nodal diameters). These modes are highly relevant for impeller vibrations as they match common excitation sources coming from the fluid such as the dynamic pressure fields caused by the rotor-stator-interaction [13]. Therefore, a vibrating disc submerged in water with a variable axial gap is studied as an abstraction of such impellers. This configuration is useful to recreate the impact of the gap between hub and upper cover on the fluid-added quantities.

Past research addressed vibrating discs for modal analysis, added mass, and added damping quantification using analytical, numerical and experimental approaches [14–22]. Nonetheless, little research exists about the use of CFD for the numerical replication of experimentally measured fluid-added damping for a standing vibrating disc in still fluid, and explaining the physics behind the fluid-added quantities in this system. Therefore, these two aspects constitute the aim of the present work.

First, the fluid damping is computed using computational fluid dynamics (CFD). Obtained in Finite Element analyses (FEA), the 3-nodal diameters (3ND) mode is imposed on the fluid-structure interface with its frequency, mode shape, and a vibration amplitude. The aim is to replicate the experimentally determined damping by Moraga et al. [23]. Therefore, the experimental configuration is recreated in the numerical model. The impact of the oscillation amplitude and of the axial gap on the added damping is studied. Factors that would impede the accuracy of the numerical results are identified and solutions are proposed. To this end, parameter studies are conducted to quantify the sensitivity of the damping prediction towards experimental and numerical uncertainties. Second, the valid numerical flow fields are visualized to gain insights into the underlying physical phenomena of the fluid-added quantities.

2. Starting point

2.1 Experimental conclusions

Constituting the experimental basis of the present work, the study of Moraga et al. [10] led to the following conclusions (Figure 1):

- The fluid damping increases with the vibration amplitude
- The fluid damping increases with the decrease of the axial gap size
- The fluid damping increases with the increase of added mass

- The increase of the fluid damping with the vibration amplitude gains significance, the lower the axial gap size

The success of the numerical simulations is assessed by their ability to recreate the experimental damping values and by their compatibility with the above-listed conclusions.

2.2 Phase-based computation and understanding of the fluid-added quantities

Based on the fluid-structure model given in equations (1) and (2), the fluid-added quantities are represented in the phase diagram in Figure 2.

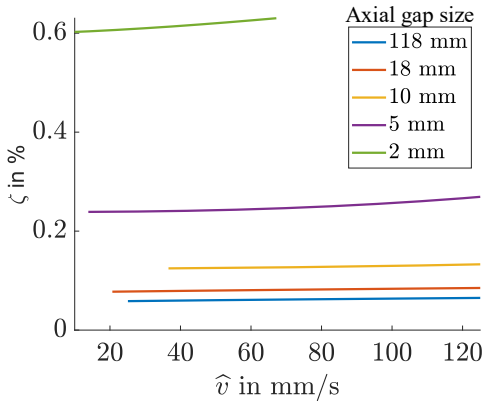


Figure 1. Experimental fluid damping ratio ζ for all axial gap sizes and velocity amplitudes $\hat{v}$ [10].

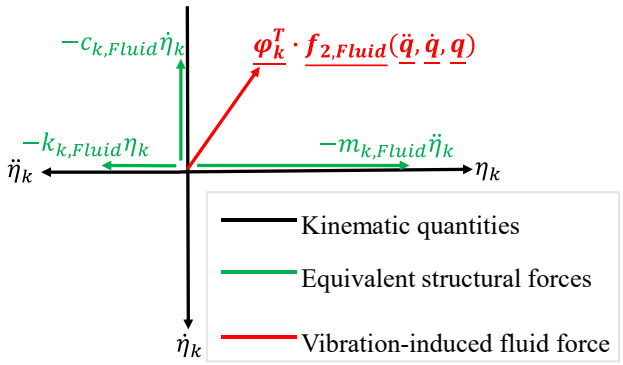


Figure 2. Fluid-added force (red) split into parts depending on the temporal phase difference to the modal displacement η_k: the fluid-added mass force $-m_{k,Fluid}\ddot{\eta}_k$, damping force $-c_{k,Fluid}\dot{\eta}_k$, and stiffness force $-k_{k,Fluid}\eta_k$.

The fluid-added forces exhibit the phase difference ψ to the structural displacement: $\psi_{mass} = 0\ rad$, $\psi_{Damping} = \pi/2\ rad$, $\psi_{Stiffness} = \pi\ rad$. Based on the given phases and a cosine-ansatz for the modal displacement η_k, the added damping ratio $\zeta_{k,Fluid}$ is computed using equation (3). Herein, ω_k, Im, FT, and $\widehat{\eta_k}$ denote respectively the eigenfrequency of the mode, the Imaginary part of a complex number, the complex Fourier transformation, and the amplitude of the modal oscillation. $\underline{f_{2,Fluid}}$ is obtained from CFD simulations with the Imposed Modal Motion Approach (IMMA hereafter).

$$\zeta_{k,Fluid} = \frac{c_k}{2 \cdot \left(m_k + m_{k,Fluid}\right) \omega_k} = -\frac{\mathrm{Im}\left\{\underline{\varphi_k}^T \mathrm{FT}\left(\underline{f_{2,Fluid}}\right)\right\}}{2 \cdot (m_k + m_{k,Fluid}) \omega_k^2 \widehat{\eta_k}} \tag{3}$$

3. Testcases

In Figure 3, a schematic of the experimental configuration is given. An example of a CFD model for the axial gap size 5 mm is illustrated in Figure 4. In table 1, information about the simulated test cases is given: The eigenfrequencies and the associated axial gap size. The simulated velocity amplitudes $\hat{v}$ can be extracted directly from the figures that contain the numerical results. The displacement amplitudes can be computed with the velocity amplitudes by division by ω_k.

Table 1. Eigenfrequencies of the submerged disc as a function of the axial gap size.

Axial gap *d* in mm	118	18	10	5	2
Eigenfrequency $\omega_k/2\pi$ in Hz	353.69	336.94	310.63	273.69	221.38

4. Results

4.1 Validation of the numerical prediction against the experimental outcome

All numerical simulations are conducted using the commercial software package Ansys (CFX, Mechanical). The first investigations are conducted for d = 118 mm and a displacement amplitude of 0.02 mm which corresponds to a velocity amplitude of 44.45 mm/s. In the IMMA simulations, incompressible flow, a mesh with 3 million elements, a limit residual of 10^{-6}, and 200 time steps per period of vibration are applied. The high-resolution advection scheme is applied. For time stepping, the second order backward Euler method is employed. Turbulence models show no impact on the results and are therefore not used. As a result, the experimental damping is overestimated by a factor of 12, as illustrated in Figure 5 (a). A time step refinement study is conducted for the current mesh until convergence of the damping value is reached. The convergence is achieved with 2000 time steps per period. As a result, the overestimation factor is significantly reduced to 3. The clear impact of the latter refinement in temporal resolution is associated with a drastic reduction of the numerical dissipation caused by the implicit integration scheme. Superimposed with the physical dissipation, the numerical dissipation falsifies the computed fluid damping (Figure 5 (a)). For a given mesh size, the courant number (CFL) is an indicator of the numerical dissipation induced by the temporal resolution. With 2000 time steps, a maximum CFL number of 0.1 is achieved which is below 1. This limit is equivalent to the Nyquist criterion required for sampling in signal processing applications. Nonetheless, the remaining overestimation (by a factor of 3) must be rooted in disparities between simulation and experiment and modelling uncertainties.

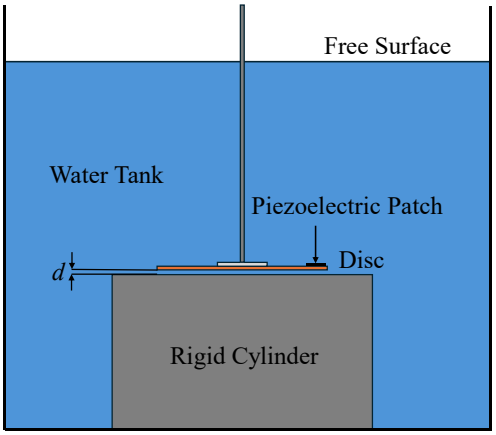


Figure 3. Schematic of the experimental configuration.

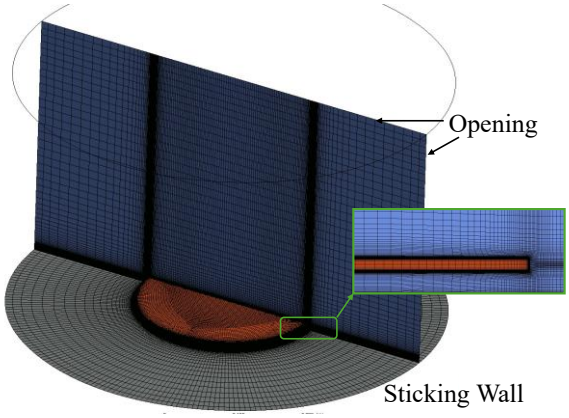


Figure 4. CFD model with a mesh of 3 million elements for the example of $d = 5\ mm$.

Moraga et al. [23] suggested that the recirculation vortices which form on the plate edge due to the flow between the upper and lower face of the disc are the root cause of the shear dissipation in the flow and consequently the fluid damping. This information points in the direction that the shape of the disc edge is key for the fluid added damping. Upon closer examination of the disc of the experiment, the edge turns out to be not perfectly sharp, yielding a discrepancy between the initial numerical model and the experiment. Since the shape of the disc edge was not deliberately designed for the experiment, it is consequently regarded as round in all the following simulations, with a radius of 0.37 mm based on an approximate measurement. As a result, the overestimation factor is further reduced to 2 (Figure 5 (a)).

Note that the low displacement amplitudes of the vibration (starting from 7.8 µm) are well into the range of manufacturing tolerances of standard sheet metal, yielding nonuniform vibrations on the disc surface. Moreover, the low amplitude vibrations and the absence of a vibration-independent convective flow lead to an overall low energy level of the system. This causes the requirement of particularly high temporal and spatial resolution to reduce the numerical dissipation to a level where it does not interfere

with the physical dissipation. Therefore, the full potential of the temporal and spatial resolution to replicate the measured damping must be explored. Before dedicating to this task, it is useful to apply the current numerical configuration to all axial gap sizes and vibration amplitudes in order to study the generality of the observations made so far. Therefore, results for all sizes of the axial gap and vibration amplitudes are illustrated in Figure 5 (b).

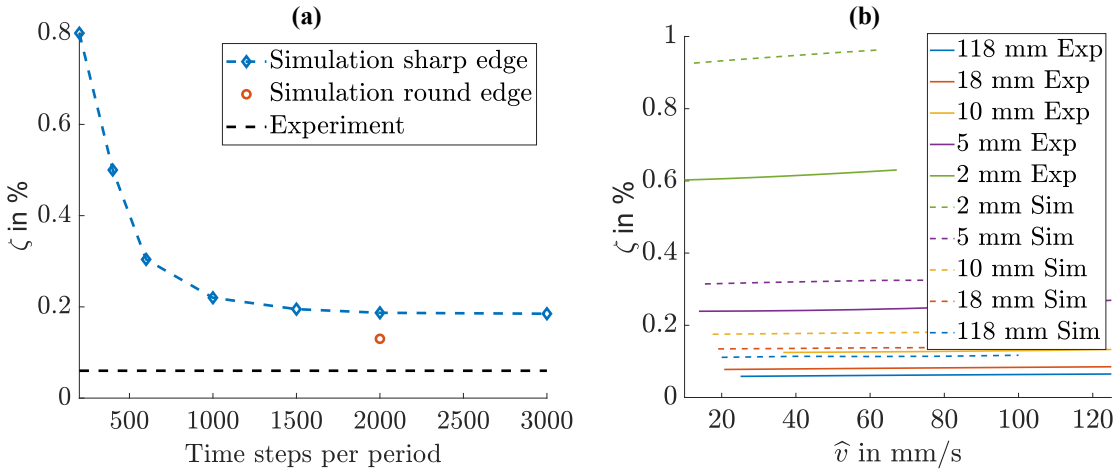


Figure 5. Comparison of the numerically predicted fluid damping with the experiment: $d = 118$ mm and $\hat{v} = 44.45$ mm/s for the disc with a sharp and rounded edge **(a),** and all wall distances and vibration amplitude for the disc with the rounded edge obtained with 2000 time steps per period **(b)**.

For all axial gap sizes, the numerically predicted fluid damping follows all the tendencies observed in the experiment: Damping increase with decrease in axial gap size, damping increase with increase of vibration amplitude, higher significance of damping increase with a vibration amplitude for lower axial gap sizes. However, a deviation in value between the predicted and the measured damping remains. Interestingly, this deviation decreases with a decrease in the axial gap size from 100 % for d = 118 mm to merely 50 % for d = 2 mm. This observation is congruent with the interference of the numerical dissipation with the physical dissipation: The lower the axial gap size, the higher the physical dissipation, the lower the requirements on the numerical discretization to maintain the numerical dissipation below interference with the physical dissipation. This underscores once more the necessity of exploring the potential of numerical resolution.

The impact of the temporal and spatial resolution on the accuracy of the predicted damping is investigated for a velocity amplitude of 40 mm/s, for both the highest axial gap size (d = 118 mm) and the lowest axial gap size (d = 2 mm). The results are depicted in Figure 6.

With a mesh size of 16 million elements and starting from 6000 time steps per period, the numerically predicted damping for d = 118 mm starts to converge towards the experimentally determined damping (Figure 6 (a)). The remaining deviation with 10000 time steps per period is limited to 6 % which is a drastic reduction compared to the 100 % with a mesh size of 3 million elements and 2000 time steps per period. In contrast, the discretization shows a much lower impact on the predicted damping for d = 2 mm. In this case, the deviation from the experiment falls from initially 50 % with 3 million elements and 2000 time steps per period to 33 % with 10 million elements and 14000 time steps. These results show that after eliminating the shortcomings of insufficient discretization, the numerical configuration recreates the physics of the fluid damping for the d = 118 mm, leading to a very good agreement with the experiment. At the same time, the simulation model seems to have remaining disparities with the experiment for d = 2 mm.

Maintaining a perfectly flat disc in the experiment (flat means that the upper and lower disc faces are parallel to the rigid wall, no tilt) proved to be a challenging task. While it shouldn't have an impact on the experimental damping with a large axial gap, the change of damping for small axial gap sizes such

as d = 2 mm can be significant, even for a small disc tilt α_{tilt} below 0.5°. The latter constitutes a further uncertainty inherent to the experimental damping. Therefore, the impact of a α_{tilt} = 0.3°disc tilt around an axis parallel to the rigid wall, tangent to the lower disc edge, and with the distance to the rigid wall equal to d is investigated. The tilt is introduced in such a way that the lowest axial gap size of the disc is equal to d (uptilt). The results are presented in Figure 7.

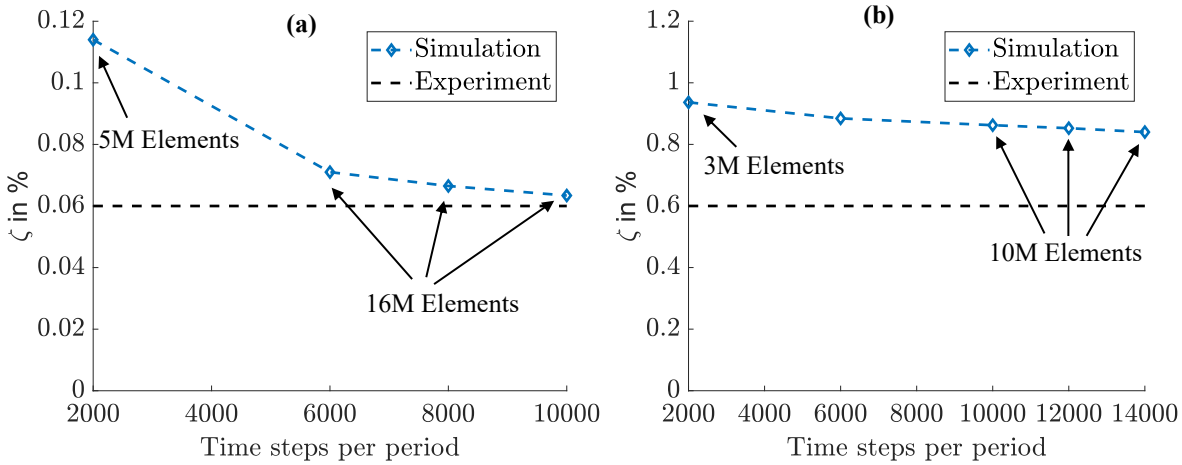


Figure 6. Impact of temporal and spatial resolution on the accuracy of the predicted damping for $\hat{v} = 40$ mm/s: $d = 118\ mm$ **(a)** and $d = 2\ mm$ **(b)**.

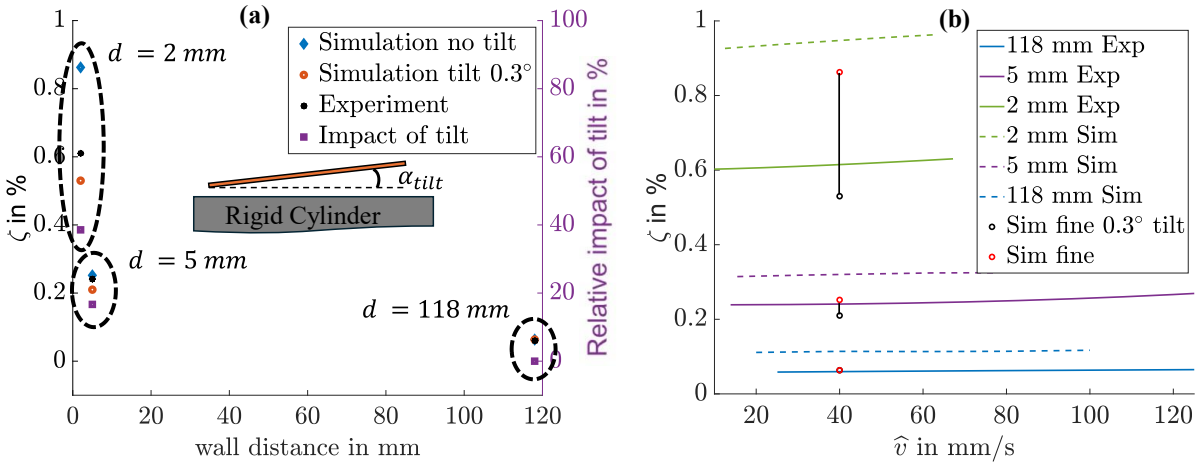


Figure 7. Impact of a tilted disc on the numerically predicted damping: Results for $\hat{v} = 40\ mm/s$ **(a)** and comparison to damping results with all vibration amplitudes **(b)**.

As expected, the introduced tilt yields no change in the predicted fluid damping for d = 118 mm. The sensitivity towards the tilt increases with a decreasing axial gap causing a significant impact of approximately 40 % for d = 2 mm (Figure 7 (a), ordinate on the right in purple). For both axial gap sizes 5 mm and 2 mm, the predicted damping for the tilted disc is lower than the experimental damping. Therefore, the numerically predicted damping falls well within the range of uncertainty of the experimental damping due to a disc tilt (Figure 7 (b)).

4.2 Visualization and explanation of the physics behind the fluid-added quantities

How does the vibration-induced flow field look like? What causes the fluid-added quantities? The goal of this section is to get to the bottom of these questions.

4.2.1 How does the vibration-induced flow field look like? (2-dimensional)

First, the oscillation sequence of the steady-state vibrations is studied and illustrated in Figure 8 (a)-(e) for d = 118 mm in the section A-A, which cuts through two vibration antinodes. When the disc is moving across the zero-deformation line at time instant t = 0, it has its maximum velocity pointing down, and so does the fluid layer immediately at the disc surface due to the stick condition between solid and fluid. At this instant, the structural acceleration and hence the fluid acceleration equal zero. Therefore, the pressure is constant all across the fluid field as flow is accelerated by pressure gradients. At t = T/8, the structure is still moving down, however with an increasing acceleration pointing up. It means that the disc is slowing down, and so is the fluid on the disc surface. Due to its inertia, the surrounding fluid

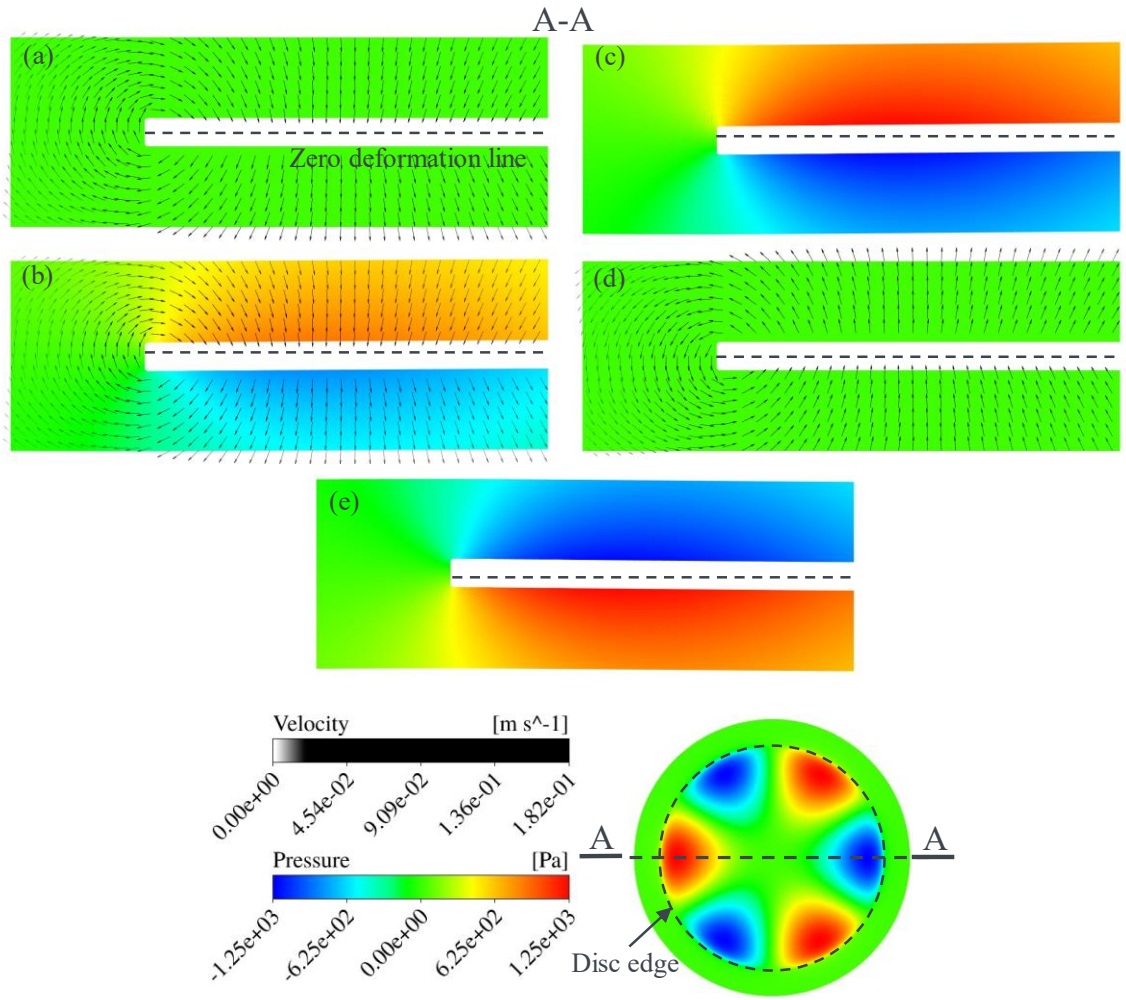


Figure 8. Pressure distribution and velocity field in the water domain near the edge of the disc [(a)-(e)] at time instants [(a): $t = 0$; (b): $t = T/8$; (c): $t = T/4$; (d): $t = T/2$; (e): $t = 3 \cdot T/4$] of an oscillation period T, for $d = 118\ mm$ and $\hat{v} = 40\ mm/s$.

opposes the resulting change of momentum by a pressure reduction on the bottom part of the disc (the fluid wants to escape the disc surface) and a pressure increase on the top side of the disc (the fluid wants to penetrate the disc surface). So, in the time window $t \in]0, T/4[$, the fluid flows against the pressure gradient. Evidently, the flow is accelerated from the high-pressure zone on the top of the disc towards the low-pressure zone on the bottom of the disc, leading it to reach standstill at t = T/4 with the maximum pressure difference between the top and the bottom face of the disc. The pressure difference keeps accelerating the fluid to flow from the bottom to the top part of the disc for $t \in]T/4, T/2[$ until the fluid

and the disc reach their maximum velocity again at t = T/2. For the rest of the period, the velocity and pressure patterns repeat with symmetry to the zero-deformation line.

4.2.2 What causes the fluid-added quantities?

Induced by the structural acceleration, the oscillating pressure force on the disc (difference between top pressure force and bottom pressure force) seems to be opposed in phase to the structural acceleration and thus in phase with the displacement, as judged by the visualizations of the flow field. However, computing the phase of the modal pressure force reveals a slight difference between the structural displacement and the pressure force ($\psi \approx 0.0035$ rad for d = 118 mm). Consequently, the oscillations of the pressure field on the disc surface primarily translate into the added mass force, however, also create a comparatively much lower damping force. The vibration-induced pressure shape follows the structural mode shape leading to a high participation factor of the pressure field in the modal force. The shear stress field oscillates with the flow velocity oscillations. Nonetheless, its lower amplitudes (at least two orders of magnitude below the pressure) and the differences of its spatial distribution compared to the mode shape yield a negligible contribution to either of the added mass and damping. Consequently, the fluid-added damping stems almost entirely from the slight phase difference between the modal pressure force and the structural displacement.

Lowering the axial gap size causes an increase of the pressure oscillation amplitude and thus a higher added mass and damping, given that the temporal phase of the pressure field remains similar. Interestingly, the latter phase difference increases to $\psi \approx 0.0194$ for d = 2 mm, skewing the pressure force toward the added damping force.

4.2.3 Flow patterns (3-dimensional)

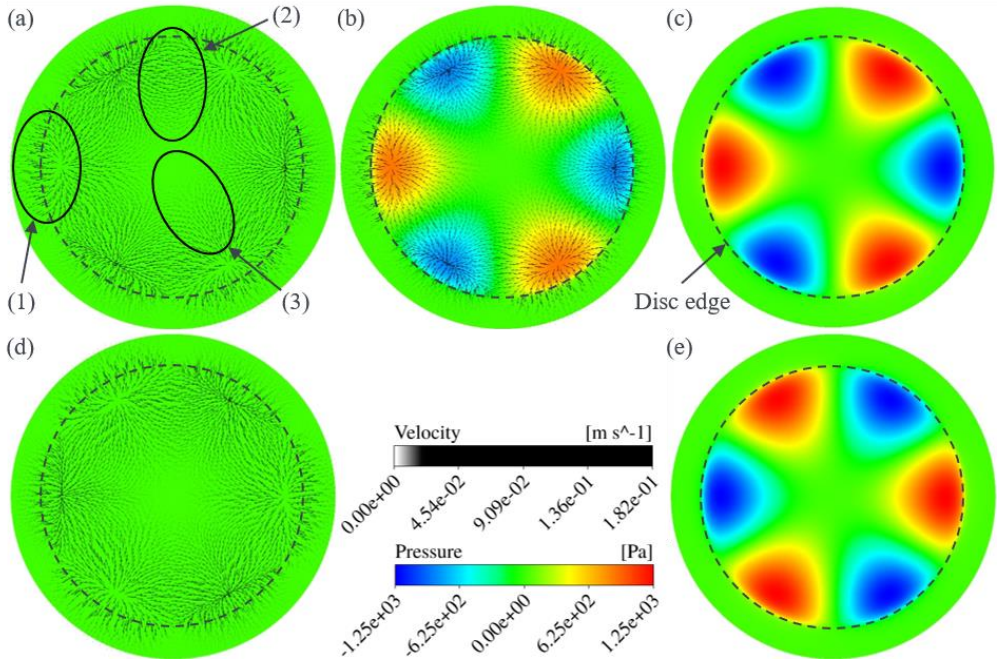


Figure 9. Pressure distribution in a plane on the upper disc surface extended to the surrounding water, and velocity field in a plane 1 mm above the disc surface at time instants [(a): $T = 0$; (b): $T = T/8$; (c): $T = T/4$; (d): $T = T/2$; (e): $T = 3 \cdot T/4$] of an oscillation period T for $d = 118\ mm$, $\hat{v} = 40\ mm/s$.

To create a more complete picture of the fluid-structure-interaction, the oscillation sequence of the velocity and pressure field is visualized on the top part of the disc in Figure 9. The temporal phase angles of pressure and velocity fit the observations made in section 4.2.2. The pressure field exhibits a mostly

similar shape to the structural mode. The drop in pressure towards the edge of the disc that is associated with the flow around the disc edge, is one noticeable difference. The maximum pressure is located in distance from the disc edge and is associated with the acceleration of the vertical flow (Figure 8 (b)), that cannot escape the disc vibrations (neither around the edge, nor to a different location on the same disc face. The circumferential component of the velocity field also follows a shape associated with the structural mode, with a relative circumferential rotation angle of 30°, which is equivalent to a quarter of the wavelength (120°) of the 3ND mode. The flow pattern on the disc face is driven by the pressure gradients and thus connects the antinodes of the 3ND mode. The direction in which the flow is accelerated depends on the "attractivity" of the neighboring zones. Starting from one antinode, one portion of the fluid is accelerated around the edge of the disc (zone (1) in Figure 9). Here the same antinode on the other disc face is the most attractive. The other portions of the fluid are accelerated respectively in the direction of the vibration antinode located clockwise/anticlockwise (zone (2)), towards the diametrically opposed antinode (zone (3)), and vertically (around the maximum pressure zone).

5. Conclusion

To study the impact of the axial gap between the hub of a radial impeller and the head cover on the fluid-added quantities, the fluid damping was numerically predicted using a combination of CFD and FEA simulations. First, the requirements for numerical simulations to accurately predict the fluid damping are identified, as evaluated by validation against the experiment. The applied numerical methodology enabled replication of the experiment with good accuracy for all axial gap sizes under consideration of the following aspects:

- The low energy level in the system due to the low vibration amplitudes and the absence of main flow yields high requirements of spatial and temporal discretization, to reduce the numerical dissipation well-below the physical dissipation.
- The lower the axial gap size, the higher the physical damping, the lower the numerical discretization requirements (mesh and time step independence reached for the lowest wall distance with coarser time step and mesh than for the highest wall distance).
- Uncertainties in the experiment, such as the ability to maintain the disc perfectly parallel to the rigid wall, and the shape of the disc edge, have major impact on the fluid-added damping.

The simulations were used to analyse the physics of the fluid-added quantities for the present system with the conclusions:

- The oscillating pressure field on the disc contributes almost entirely to the fluid-added mass.
- The fluid-added damping is almost entirely caused by the slight phase difference between the modal pressure force and the structural displacement caused by friction in the fluid. The contributions of the shear stress field to added mass and damping remain negligible due to the low shear stress amplitudes and the spatial mismatch between the shear stress field and the structural mode shape.
- The phase angle between the modal pressure force and the modal displacement increases with a decreasing gap size, skewing the pressure force more towards added damping.

Future work can focus on analysing the impact of disc rotation on the fluid-added quantities, aiming at valid numerical simulations, study configurations that are closer to hydraulic impellers, explain the dependence of the fluid-added quantities on boundary conditions (wall distance) using flow physics, and address many more open questions.

References

[1] Seidel U, Mende C, Hübner B, Weber W, Otto A. Dynamic loads in Francis runners and their impact on fatigue life. IOP Conf. Ser.: Earth Environ. Sci. 2014;22(3):32054.
[2] Valero C, Egusquiza M, Egusquiza E, Presas A, Valentin D, Bossio M. Extension of Operating Range in Pump-Turbines. Influence of Head and Load. Energies 2017;10(12):2178.

[3] Nennemann B, Monette C, Chamberland-Lauzon J. Hydrodynamic damping and stiffness prediction in Francis turbine runners using CFD. IOP Conf. Ser.: Earth Environ. Sci. 2016;49:72006.
[4] Valentín D, Presas A, Valero C, Egusquiza M, Jou E, Egusquiza E. Influence of the hydrodynamic damping on the dynamic response of Francis turbine runners. Journal of Fluids and Structures 2019;90:71–89.
[5] Bergan CW, Tengs EO, Solemslie BW, Dahlhaug OG. An experimental investigation of the hydrodynamic damping of vibrating hydrofoils. IOP Conf. Ser.: Earth Environ. Sci. 2019;240:62008.
[6] Bergan CW, Solemslie BW, Østby P, Dahlhaug OG. Hydrodynamic Damping of a Fluttering Hydrofoil in High-speed Flows. IJFMS 2018;11(2):146–53.
[7] Coutu A, Seeley C, Monette C, Nennemann B, Marmont H. Damping measurements in flowing water. IOP Conf. Ser.: Earth Environ. Sci. 2012;15(6):62060.
[8] Gauthier JP, Giroux AM, Etienne S, Gosselin FP. A numerical method for the determination of flow-induced damping in hydroelectric turbines. Journal of Fluids and Structures 2017;69:341–54.
[9] Liaghat T, Guibault F, Allenbach L, Nennemann B. Two-Way Fluid-Structure Coupling in Vibration and Damping Analysis of an Oscillating Hydrofoil.
[10] Tengs EO, Bergan CW, Jakobsen K-R, Storli PT. Numerical simulation of the hydrodynamic damping of a vibrating hydrofoil. IOP Conf. Ser.: Earth Environ. Sci. 2019;240:62002.
[11] Tengs E, Einzinger J, Storli P-T. Two-way coupled simulation of the Francis-99 hydrofoil using model order reduction. J. Phys.: Conf. Ser. 2019;1296(1):12001.
[12] Østby PTK, Agnalt E, Haugen B, Tore Billdal J, Gunnar Dahlhaug O. Fluid structure interaction of Francis-99 turbine and experimental validation. J. Phys.: Conf. Ser. 2019;1296(1):12006.
[13] Hübner B, Weber W, Seidel U. The role of fluid-structure interaction for safety and life time prediction in hydraulic machinery. IOP Conf. Ser.: Earth Environ. Sci. 2016;49:72007.
[14] Amabili M. effect of finite fluid depth on the hydroelastic vibrations of circular and annular plates. Journal of Sound and Vibration 1996;193(4):909–25.
[15] Amabili M, Frosali G, Kwak MK. free vibrations of annular plates coupled with fluids. Journal of Sound and Vibration 1996;191(5):825–46.
[16] Askari E, Jeong K-H, Amabili M. Hydroelastic vibration of circular plates immersed in a liquid-filled container with free surface. Journal of Sound and Vibration 2013;332(12):3064–85.
[17] Hengstler J, Dual J. Fluid structure interaction of a vibrating circular plate in a bounded fluid volume: simulation and experiment:3–10.
[18] Presas A, Valentin D, Egusquiza E, Valero C, Seidel U. Dynamic response of a rotating disk submerged and confined. Influence of the axial gap. Journal of Fluids and Structures 2016;62:332–49.
[19] Presas A, Valentin D, Egusquiza E, Valero C, Seidel U. Influence of the rotation on the natural frequencies of a submerged-confined disk in water. Journal of Sound and Vibration 2015;337:161–80.
[20] Valentín D, Presas A, Egusquiza E, Valero C. Influence of the added mass effect and boundary conditions on the dynamic response of submerged and confined structures. IOP Conf. Ser.: Earth Environ. Sci. 2014;22(3):32042.
[21] Weder M, Horisberger B, Monette C, Sick M, Dual J. Experimental modal analysis of disk-like rotor–stator system coupled by viscous liquid. Journal of Fluids and Structures 2019;88:198–215.
[22] Louyot M, Nennemann B, Monette C, Gosselin FP. Modal analysis of a spinning disk in a dense fluid as a model for high head hydraulic turbines. Journal of Fluids and Structures 2020;94:102965.
[23] Moraga G, Xia X, Roig S, Valero C, Valentín D, Egusquiza M et al. Experimental study on the influence of vibration amplitude on the fluid damping of a submerged disk. Journal of Sound and Vibration 2024;569:118099.